



Flameout and Combustion Efficiency of Scramjet-Powered Hypersonic Vehicles During Ascent

Chukwuka C. Mbagwu*, James F. Driscoll†

As a hypersonic vehicle travels to high altitudes along an ascent trajectory, the static pressure (p_3) in the scramjet combustor will decrease, which can lead to engine flameout and lower combustion efficiency. At low pressures the chemical reactions between the fuel and air become excessively slow. However, during the ascent the flight Mach number is increasing so there is an increase in the stagnation temperature and the static temperature (T_3) at the combustor entrance. This tends to prevent flameout and to improve combustion efficiency. To investigate the tradeoff, a reduced-order model called MASIV first was used to compute the static temperature and pressure at the entrance to the combustor (T_3, p_3) as a function of altitude for a trimmed vehicle. Then the combustion efficiency was computed using the finite-rate chemistry sub-model. To determine if flameout occurs at each altitude, values of (T_3, p_3) are inserted into an empirical relation that includes the measured value of the critical Damkohler number. Three empirical constants are selected so that the model predictions agree with available measured values combustion efficiencies and flameout limits.

The reduced-order model approach provides rapid (but approximate) answers that are useful when thousands of computations are needed for optimization studies or to develop a control algorithm. Results are plotted as three curves on a graph of vehicle altitude versus flight Mach number. The first curve is the vehicle trajectory; the second curve is the combustion efficiency versus altitude and the third curve is the flameout limit. The trajectory curve was optimized to stay near the highest efficiency curves while not intersecting the flameout limit curve. Another optimization study identified the optimum number of wall-port fuel injectors.

Nomenclature

S_b	=	burning velocity [m/s]
U_3	=	air velocity at combustor entrance [m/s]
U_F	=	fuel jet velocity [m/s]
f_s	=	stoichiometric mixture fraction
S_T	=	turbulent burning velocity [m/s]
S_L	=	stretched laminar burning velocity [m/s]
S_L/S_{L0}	=	non-dimensional stretch factor
Ka	=	Karlovitz number
d_F	=	fuel jet diameter [m]
p_3	=	pressure at combustor inlet [Pa]
T_3	=	temperature at combustor inlet [K]
U_3	=	velocity entering the combustor [m/s]
Da	=	Damkohler number

I. Introduction

Consider the hypersonic wave rider that is shown in Figure 1. This vehicle, called MAX-1 [1], ascends along the constant dynamic pressure trajectory (the solid line) in Figure 2, which is a plot of altitude versus flight Mach number. It is desired to compute a second curve that is the engine flameout operability limit; this limit is sketched as the dotted line in Figure 2. The trajectory curve then can be modified so as to avoid the flameout limit curve. For example, in a dual-mode ramjet-scramjet engine it is known that whenever the static pressure at the combustor entrance becomes too small (typically less than 0.5 atm.) then flameout is possible. However, static pressure is only one of several parameters that govern flameout.

The solid curve in Figure 2 represents a constant dynamic pressure ($q = \frac{1}{2}\rho_\infty U_\infty^2 = 100$ kPa) trajectory. As the vehicle flight Mach number increases from 4.4 to 7.0 along this trajectory, the altitude must increase from 18 km to 24 km. It can be shown that for a constant q ascent trajectory, the ambient pressure (p_∞) will decrease and is

*Ph.D. Candidate, Dept. of Aerospace Engineering, Univ. of Michigan, USA, AIAA Member, cmbagwu@umich.edu

†Professor, Dept. of Aerospace Engineering, Univ. of Michigan, USA, AIAA Fellow, jamesfd@umich.edu

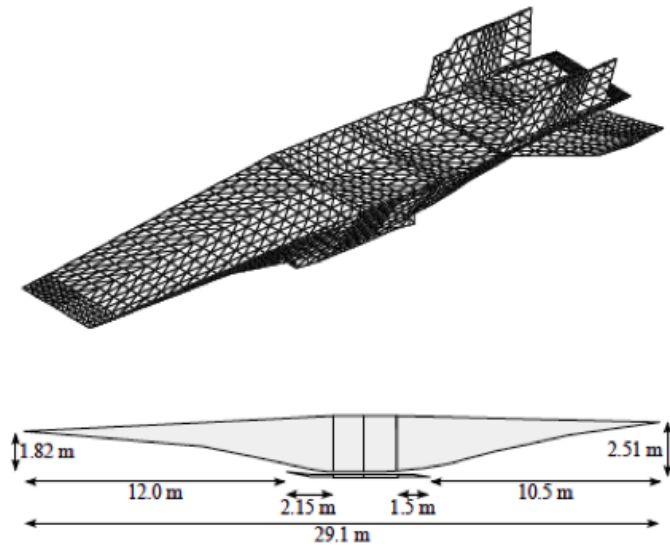


Figure 1. MAX-1 vehicle and flow path dimensions. Engine width is 2.143 m.

proportional to $(1/M_\infty^2)$. For the special case of an inlet that provides a constant compression ratio (p_3/p_∞), it follows that combustor pressure p_3 will also be proportional to $(1/M_\infty^2)$. Thus, increasing the Mach number from 4.4 to 7.0, as sketched in Figure 2, leads to a nearly threefold increase in the combustor pressure. This can cause such a large decrease in the chemical reaction rate of the fuel chemistry that the result is engine flameout.

The dotted line in Figure 2 is a sketch of a possible flame out limit of the vehicle; this curve is derived in section VIII. It is not a general result but rather depends on the specific geometry of the flame holder and the engine flow path. It has a shape that shows that flying at excessively high altitudes leads to flameout due to very small combustor pressures. Also, as flight Mach number increases, the stagnation temperature becomes so large that the air static temperature exceeds the auto-ignition temperature. A flame holder is no longer necessary, but flameout can still occur if the ignition delay time exceeds the residence time that the fuel-air mixture spends in the combustor section.

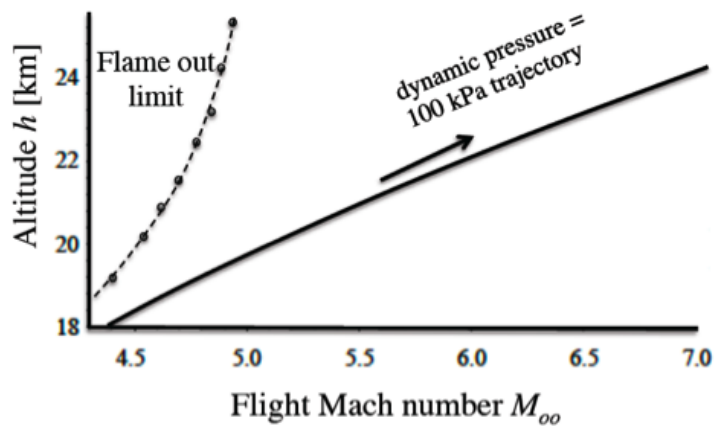


Figure 2. Schematic of a possible flameout limit (dotted line), and a selected vehicle ascent trajectory (solid line, $q = 100$ kPa).

II. Approach

In order to compute the flameout limit, it is necessary to first assume that a wall-cavity flame holder is employed, and then use an empirical relation for the measured critical Damkohler number at flameout. This approach has been used to estimate flameout limits in afterburners, using the Ozawa empirical flameout relation [2] or a similar empirical relation [3–7]. Damkohler number [2, 5, 8] is an important propulsion parameter that is defined to be:

$$Da_H = \frac{RR_F(ER, p_3, T_3)}{U_3/H} \quad (1)$$

The characteristic length scale is the height (H) of the wall-cavity. Cavity flame holders have been studied extensively [8–13]. RR_F is the maximum reaction rate of the fuel (in 1/seconds) that is defined in Section V below. It depends on the equivalence ration (ER), static pressure (p_3) and static temperature (T_3). Station 3 is defined to be the combustor entrance; station 1 is the leading edge of the vehicle and station 2 is the entrance to the constant-area isolator portion of the inlet (as shown in Figure 3). U_3 is the air velocity at the combustor entrance.

The critical value of Damkohler number (Da_H^*) that causes flameout must be determined from experiments because no CFD computations can reliably compute this value. Fortunately there are many measured values for a cavity flame holder already available. Next the quantity U_3^* is defined; it is the maximum air velocity at the combustor entrance that is allowed before flameout will occur. A formula for U_3^* is determined by rearranging equation (1):

$$U_3^* = \frac{RR_F}{Da_H^*} H \quad (2)$$

As the vehicle ascends, the air velocity U_3 at the combustor entrance will increase. When the velocity U_3 equals the right side of equation (2), flameout occurs. So, the flameout limit is designed to be:

$$U_3 = U_3^* \quad (3)$$

Therefore, equations (2) and (3) are the primary relations that are used to compute the flameout limit. However, the right side of equation (2) changes during ascent and must be computed at each altitude along the trajectory. The reason why U_3 increases during the ascent is that the increase in the free stream Mach number (from 4.4 to 7.0 in Figure 2 causes the inlet stagnation temperature to increase. This raises the static temperature T_3 at the combustor entrance, as well as the local speed of sound, and this tends to increase U_3 . The cavity flame holder in the MAX-1 vehicle is assumed to be a scaled up version of the experiment of Gruber et al. [9], who found that lean flameout occurs when $U_3 = 100$ m/s, $H = 0.7$ cm, and RR_F , based on the computations below, is 100 s⁻¹. Therefore the measurements indicate that Da_H^* equals 100 .

Table 1. Measured values of critical Damkohler number (Da_H^*) for a cavity-stabilized flame in a scramjet combustor, as reported by AFRL and other researchers [8,9,11,12,14]

Critical Damkohler #	
Gruber	$Da_H^* = \dots$
Rasmussen	$Da_H^* = \dots$
Driscoll	$Da_H^* = \dots$
Donohue	$Da_H^* = \dots$

III. Previous Related Work

This section is a brief summary of previous reduced-order models (ROMs) of hypersonic vehicles. A reduced order model is one that rapidly accesses pre-computed lookup tables; the lookup tables were generated using CFD codes for one particular geometry or for the chemical kinetics of one type of fuel.

In 2006, the Bolender-Doman AFRL model [15, 16] simulated the flight dynamics of a hypersonic vehicle but it neglected many details of the propulsion system. To improve the AFRL model, a joint effort between the University of Michigan and AFRL led to the MASIV (Michigan-AFRL Scramjet In-Vehicle) second-generation model [1, 17–20]. Items that were added include multiple interacting shock waves in the 2-D inlet (and the exhaust nozzle) using a technique similar to the method of characteristics and 3-D fuel-air mixing. 3-D mixing was added by included experimentally-measured formulas for the variation of mixture fraction within a fuel jet that is injected into an air cross-flow. Also added was finite-rate chemistry, by including strained flamelet lookup tables similar to those used in the CFD code FLUENT. A trim code was added to compute lift, drag and moments in order to trim the vehicle at the proper angle of attack at each altitude during the ascent. This work led to a series of publications, one of which demonstrated that the MASIV code can compute the optimum acceleration time-history that minimizes the fuel required for ascent [1]. MASIV also was used to compute the ram-scram transition boundary [1] and the operability limit where the initial stages of engine unstrap occurs. Other reduced-order models of hypersonic vehicles have been reported by O'Neill and Lewis [21]. Bowcutt [22] and others [23–27] developed models for untrimmed vehicles

that are operated far from the flameout limit. However, no previous reduced-order model has attempted to compute flameout. So the new aspects of this work are that it provides a methodology for computing the engine flameout limits, and the methodology can be applied to a trimmed vehicle undergoing an ascent trajectory to generate operability limits, such as the dotted line in Figure 2.

There is a strong motivation to develop reduced-order models for hypersonic vehicles. A ROM provides an approximate solution rapidly; they are commonly used in the design of a control algorithm or to obtain a first estimate of an optimal aircraft design. A ROM also gives a “first look” at a large parameter space. The ROM can identify certain optimal conditions; at a later time, relatively few high-fidelity CFD runs then can be performed. The MASIV code computes aerodynamic forces and engine thrust for the MAX-1 wave rider by solving ordinary differential equations in less than five seconds on a single 2.6 GHz processor. With multiple processors the computational time drops to a fraction of a second.

Suppose that it is desired to compute the aircraft forces, moments, and the trimmed angle of attack at each point along six possible trajectories to determine the optimum trajectory. Forces on the vehicle must be computed approximately 1800 times. This is because for each trajectory the vehicle must be trimmed at approximately twenty different altitudes. At each altitude the forces have to be computed about fifteen times to determine (by iteration) what angle of attack, equivalence ratio, and elevator settings lead to the trim of the vehicle. A ROM does not compete against high-fidelity CFD, but instead complements it. The full CFD solution is more accurate than the reduced-order model solutions, but CFD is not appropriate early in the design cycle, where thousands of combinations of flight conditions and control inputs are needed for quick performance analysis on ascent trajectories, vehicle design optimization, and control applications.

Two disadvantages of a reduced-order model are that the level of accuracy of the ROM must be determined by validation studies, and the ROM is only valid for the one specific geometry for which the lookup tables were generated. In this case, only quasi-steady changes are considered. There are two types of ROMs: one interpolates between full-order CFD solution snapshots, and the other is used here in MASIV. MASIV is a first-principles ROM that solves the fundamental conservation equations. While 2-D or 1-D assumptions are employed, still it is possible to investigate the physics to better understand any interesting model predictions.

IV. The MAX-1 Hypersonic Vehicle

The MAX-1 wave rider is drawn in Figure 1; it is similar to the generic aircraft that was first considered by Bolender and Doman [15]. It has a length of 29.1 m and the width of the dual mode ramjet-scamjet is 2.143 m. The inlet is rectangular with a sufficiently large aspect ratio of 15.3 such that it can be considered to be two-dimensional. The isolated is 1.38 m long and is folioed by the constant area portion of the combustor that is 0.90 m long. Both have a cross section of 0.14 m by 2.143 m. The second part of the combustor is 0.62 m and it's upper wall diverges at 4 degrees.

In previous studies the sizes of the control surfaces were optimized, the weight distribution altered, and aero-elastic properties were added [1, 16–20]. Forces on each surface panel are computed using a small-angle panel method [15] and the method to trim the vehicle is described in [1]. The engine inlet is drawn in Figure 1b and it contains multiple shock waves that interact. A code called SAMURI, described in [17], is used to compute the static pressure rise and the stagnation pressure loss in the inlet and exhaust nozzle. It assumes that the flow is 2-D, wall deflection angles are small, no separation occurs, and that the supersonic inlet Mach number is small enough that strong shock/boundary layer interactions do not occur.

V. MASIV Combustor Model

The MASIV combustor code was described in detail in [18]. This code includes finite-rate chemistry, real gas properties, a three-dimensional jet mixing model, a separated boundary layer model, and gas dissociation. The air stream is modeled as a 1-D flow in the duct drawn in Figure 3. It has variable area, friction, wall heat transfer and head addition due to combustion. A 3-D pattern of fuel jets in a cross flow is superimposed on this 1-D flow. Fuel is injected from 30 ports that are located at one x-location that is 0.14 m downstream of station 3 in Figure 3. The 30 fuel jets are located at different span-wise locations across the 2.143 m width; each port is 3.45 cm in diameter. Each port is choked and the hydrogen fuel enters the combustor at 300K at the sonic speed of 1295 m/s.

MASIV solves the following seven ordinary differential equations, which include the conservation of mass (4), momentum (5), energy (9), and species (10). The equations are derived in [18].

$$\frac{1}{\rho} \frac{d\rho}{dx} = \frac{1}{\dot{m}} \frac{d\dot{m}}{dx} - \frac{1}{u} \frac{du}{dx} - \frac{1}{A} \frac{dA}{dx} \quad (4)$$

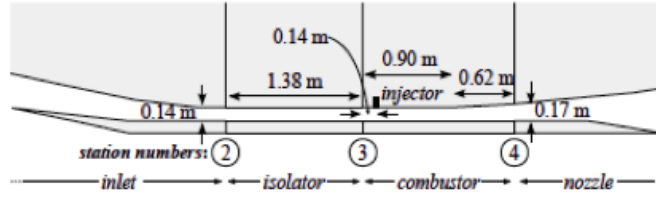


Figure 3. Dual-mode ramjet-scrumjet internal flow path of MAX-1 wave rider.

$$\frac{1}{u} \frac{du}{dx} = -\frac{1}{\rho u^2} \frac{dp}{dx} - \frac{2c_f}{D} + \left(1 - \frac{u_F}{u}\right) \frac{1}{\dot{m}} \frac{d\dot{m}}{dx} \quad (5)$$

$$\frac{1}{p} \frac{dp}{dx} = \frac{1}{\rho} \frac{d\rho}{dx} + \frac{1}{T} \frac{dT}{dx} - \frac{1}{W} \frac{dW}{dx} \quad (6)$$

$$\frac{1}{W} \frac{dW}{dx} = -\sum_{i=1}^{n_{sp}} \frac{W}{W_i} \frac{dY_i}{dx} \quad (7)$$

$$\frac{d\dot{m}}{dx} = \sum_{i=1}^{n_{sp}} \frac{d\dot{m}_{i,F}}{dx} \quad (8)$$

$$c_p \frac{dT}{dx} = \frac{h_{0,F} - h_0}{\dot{m}} \frac{d\dot{m}}{dx} - \frac{2c_f c_p (T_{aw} - T_w)}{\text{Pr}^{2/3} D} - u \frac{du}{dx} - \sum_{i=1}^{n_{sp}} h_i \frac{dY_i}{dx} \quad (9)$$

$$\frac{dY_i}{dx} = \frac{\bar{\omega}_i W_i A}{\dot{m}} + \frac{1}{\dot{m}} \frac{d\dot{m}_{i,F}}{dx} - \frac{Y_i}{\dot{m}} \frac{d\dot{m}}{dx} \quad (10)$$

Equations (6) and (7) define the equation of state and the molecular weight (W) of the gas mixture, respectively. Equation (8) states that the total mass flow rate is that of the air plus injected fuel.

An important quantity is $\bar{\omega}_i$ that appears in equation (10). It is the volumetric reaction rate of each species, in moles/sec/m³. The bar denotes that it has been averaged over the y and z directions so that it is only a function of the stream wise coordinate x . To compute the volumetric reaction rate $\bar{\omega}_i$, a 2-D empirical sub-model for the fuel-air mixing and combustion was developed, because mixing cannot be properly simulated in one dimension. The 3-D mixing model is described in [28]. First it is assumed that the fuel is injected as a jet in a cross-flow. Experiments show that the centerline of the fuel jet bends over such that its y -coordinate (y_C) is proportional to $(x_C)^{1/3}$, as given in [18–20]:

$$\frac{y_C}{d_F} = c_2 \left(\frac{x_C}{d_F} \right)^{1/3} R^{2/3} \quad (11)$$

where x_C is the axial distance from the injector, d_F is the fuel jet diameter, and R is the fuel jet momentum ratio $[(\rho_F U_F^2)/(\rho_A U_A^2)]^{1/2}$. Measurements also show that along the curved jet centerline, the mean fuel mass fraction ($Y_{F,C}$) is:

$$Y_{F,C} = c_3 \left(\frac{\rho_F}{\rho_A} \right)^{1/3} \left(\frac{u_F}{u_A} \right)^{-1/3} \left(\frac{x_C}{d_F} \right)^{-2/3} \quad (12)$$

The mean fuel mass fraction (Y_F) also varies in the direction that is normal to the curved jet centerline; experiments show that this variation is nearly Gaussian in shape. Figure 4b shows the resulting contours of hydrogen reaction rate in an x - y plane.

To account for 3-D turbulent mixing, the same mixing equations are used that appear in the CFD code FLUENT for an assumed-PDF model. At each (x, y, z) location in Figure 4b the mean mixture fraction is known, based on the empirical formulas stated above. Mixture fraction is related to the fuel mass fraction. Using the assumed-PDF approach, fluctuations in mixture fraction are assumed to be proportional to the gradient in the mean mixture

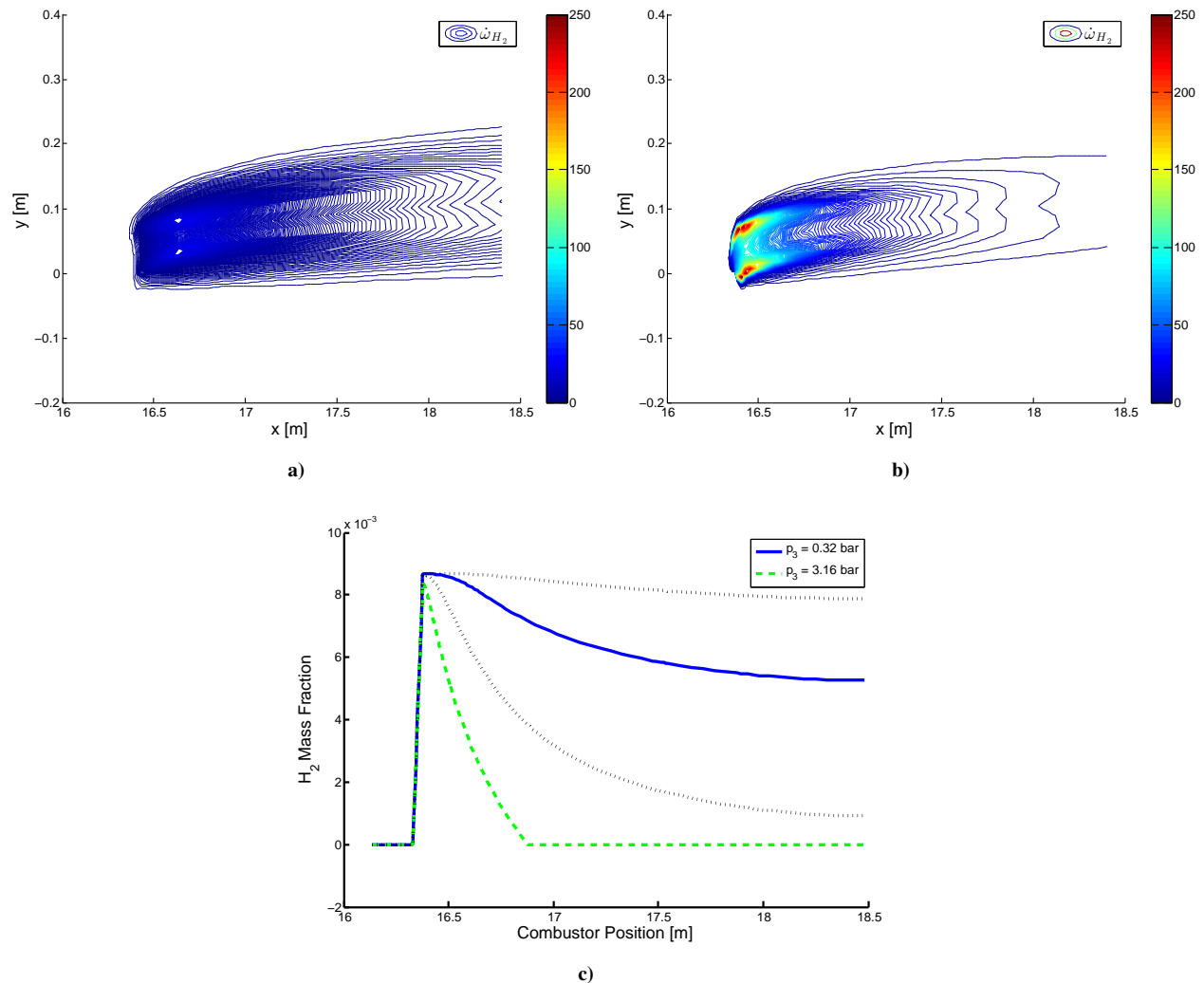


Figure 4. (a,b) Contours of volumetric reaction rate of hydrogen (ω_{H_2}), and (c) the 1-D profiles of hydrogen mass fraction (Y_{H_2}) across combustor. Two values of combustor static pressure (p_3) are considered. $T_3 = 900K$.

fraction. Another relation is used to compute the scalar dissipation rate from these fluctuations. As with the FLUENT approach, flamelet lookup tables are required to quantify the finite-rate chemistry. These were generated with the Stanford FLAMEMASTER code. This code considers strained flamelets and computes the volumetric reaction rate of hydrogen (ω_{H_2}) in moles/sec/m³ at each (x, y, z) location in the jet in cross flow.

The FLAMEMASTER code was run to create sixteen chemistry lookup tables that correspond to four combustor entrance static pressures (p_3 of 0.1, 0.32, 1.0, and 3.16 bar) and four combustor entrance static temperatures (T_3 of 500, 900, 1300, and 1700 K). During the vehicle ascent the values of p_3 and T_3 varied continuously, so the chemistry lookup tables were interpolated using the POD method described in section VI. Then these 3-D profiles are integrated to determine $\bar{\omega}_{H_2}$ from the following equation:

$$\bar{\omega}_{H_2}(x) = \frac{1}{A} \iint \omega_{H_2}(x, y, z) dy dz \quad (13)$$

This value is the reaction rate required in equation (10). Then equations (4-12) were solved to determine how rapidly the hydrogen fuel was consumed in the flow direction downstream of the fuel port.

Figure 4a and 4b show 2-D slices of the 3-D profiles of the volumetric reaction rate of hydrogen at two pressures: $p_3 = 0.32$ and 3.16 bar, respectively. The empirical equations (11) and (12) for a jet in a cross-flow were used along with the chemistry lookup tables. Notice that hydrogen mass fraction (Figure 4c) is largest just above the sidewall fuel port at $x = 16.4$ m, and it decreases downstream as the hydrogen is consumed by chemistry and mixing.

Resulting profiles of $\bar{\omega}_{H_2}(x)$ appear in Figure 5. The values of reaction rate in Figure 4a and 4b were integrated over each transverse (y, z) plane to yield an integrated hydrogen reaction rate that is only a function of x , the stream wise coordinate. The curve marked $p_3 = 3.16$ bar represents the highest pressure condition, and it follows that the reaction is the greatest. The lower pressure curve at $p_3 = 0.32$ bar has a much lower peak reaction rate; this confirms the general rule that combustor pressure should be maintained at greater than 0.5 bar for proper operation of a hypersonic propulsion system. This requires sufficient compression of the air in the inlet from a low ambient pressure up to the desired combustion pressure. The integrated reaction rate profiles in Figure 5 are the profiles that are input into the first term on the right side of equation (10).

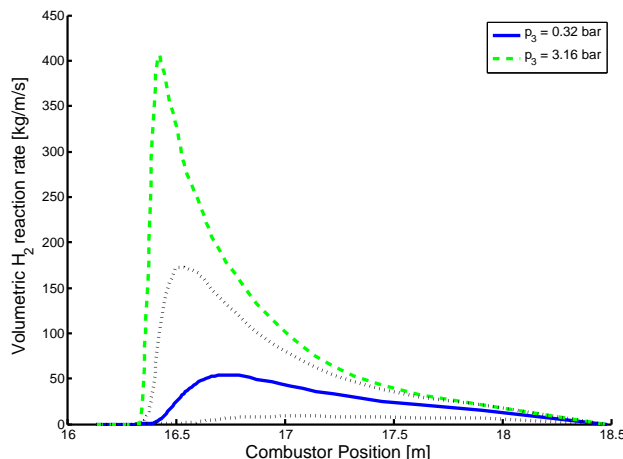


Figure 5. The 1-D profiles of volumetric hydrogen reaction rate ($\bar{\omega}_{H_2}(x)$) determine by integrating the profiles in Figure 4 over the y - z plane.

The final step is to compute the maximum fuel reaction rate (RR_F) that is defined to be:

$$RR_F = [\bar{\omega}_{H_2}(x)]_{max} \left(\frac{W_{H_2}}{\rho_{H_2}} \right) \quad (14)$$

The first term on the right $[\bar{\omega}_{H_2}(x)]_{max}$ is the maximum value of the curve drawn in Figure 5. Also appearing in equation (14) are the known values of the molecular weight of hydrogen (W_{H_2}), which is 2.016 g/mole, and the density of the injected hydrogen (ρ_{H_2}).

VI. Interpolation of Chemistry Tables using Proper Orthogonal Decomposition (POD)

With a reduced-order modeling (ROM) approach, the first task is to perform time-consuming calculations of lookup tables that contain the information about finite-rate chemistry. The large tables contain values of chemical reaction rates of nine different species as a function of many variables, including pressure, incoming air temperature, mean mixture fraction and scalar dissipation rate. These tables are similar to ones generated by the commercial code FLUENT. The chemical reaction rates were computed using the Stanford FLAMEMASTER flamelet code. The hydrogen fuel chemistry involved nine species ($H_2, O_2, H_2O, H, OH, O, HO_2, H_2O_2, N_2$) and 24 elementary reactions. Sixteen large chemistry lookup tables were generated using the above approach. Each chemistry table corresponds to one of four different combustor inlet pressures and one of four inlet temperatures. Each table contains the reaction rates of eight major species as a function of mixture fraction and fluctuations in mixture fraction. Since the combustor inlet pressure and temperature usually falls in between the values and ranges of the generated lookup tables, a rapid interpolation method is required to determine correct reaction rates.

For such a large data set, standard interpolation methods between tables for pressures and temperatures were too slow or inaccurate, so the method of POD was applied and found to be rapid and accurate. The advantages and scalability of this technique are explored, and select comparisons are made of the full, non-reduced flamelet data to the results of the POD analysis.

The proper orthogonal decomposition (POD) is a well-defined method of producing reduced-order, but very accurate, models of large or complex data sets. It has been used in computational fluid dynamics (CFD) analysis to examine correlations of the structure of turbulent flowfields in time [29–31]. Other time-domain applications include constructing reduced-order models (ROM) of cylinder vortex shedding [32] and an aeroelastic model of a two-dimensional

airfoil [33]. Analogous frequency-domain POD techniques have been explored by Kim [34], applied to a spring damper system and three-dimensional vortex lattice model. ROMs constructed using POD have been combined with structural dynamic models and applied to aeroelastic systems [35,36]; it has also been found effective for flutter analysis [37,38]. It has also been used for reduced-order models of atmospheric and oceanographic data, where the control space is high-dimensional [39]. However, in this work, the application of POD techniques to reduce multidimensional flamelet chemistry data used in a model for the mixing and combustion of turbulent jets in crossflow is explored.

Finally, using the developed POD architecture, various thermal properties and combustion efficiencies are calculated over a wide range of combustor operation conditions. As a hypersonic vehicle travels upward along an ascent trajectory, the static pressure in the scramjet combustor will decrease, which can lead to engine flameout. At low pressures the chemical reactions between the fuel and air become excessively slow. However, during ascent the flight Mach number is increasing. This increases the stagnation and static temperatures at the combustor entrance, tending to prevent flameout. These trends are observed and provide insight to determine flameout limits and ultimately flight trajectory envelopes for a hypersonic vehicle. Such results using simple and reduced models prove useful for rapid design and trajectory optimization.

VII. Results (a): Combustion Efficiencies

Combustion efficiency (η_C) is defined to be:

$$\eta_C = \frac{\dot{m}_{H_2, burned}}{\dot{m}_{H_2, inj}} = \frac{\dot{m}_{H_2, inj} - \dot{m}_{H_2, 4}}{\dot{m}_{H_2, inj}} \quad (15)$$

where $\dot{m}_{H_2, inj}$ is the mass flow rate of the hydrogen fuel injected from the wall ports. The quantity $\dot{m}_{H_2, 4}$ on the right side of equation (15) is the mass flow rate of unburned hydrogen out the exit of the combustor (station 4); it is replaced with $(Y_{H_2, 4} \dot{m}_4)$ where $Y_{H_2, 4}$ is the mass fraction of hydrogen at the combustor exit. The exit mass flow rate (\dot{m}_4) is replaced with $(\dot{m}_3 + \dot{m}_{H_2, inj})$ where \dot{m}_3 is the entering air mass flow rate. The equivalence ratio (ER) is defined to be:

$$ER = \frac{\dot{m}_{H_2, inj}}{\dot{m}_3 r_s} \quad (16)$$

The stoichiometric fuel-air ratio for hydrogen fuel (r_s) is 0.029. When the above relations are combined, it follows that the combustion efficiency becomes:

$$\eta_C = 1 - \left(\frac{Y_{H_2, 4}}{r_s ER} \right) (1 + r_s ER) \quad (17)$$

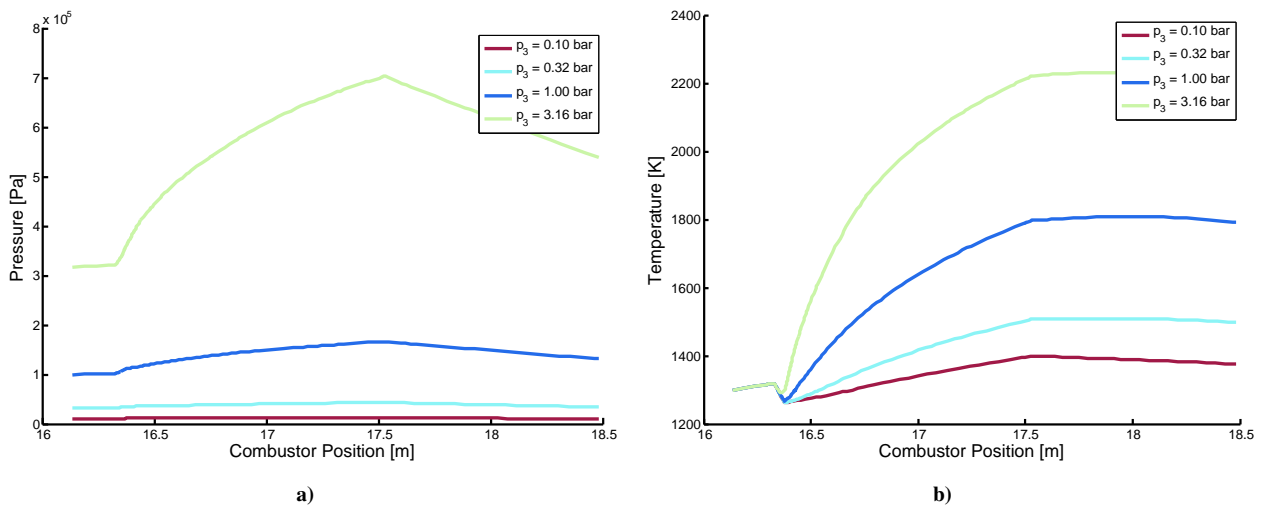


Figure 6. Static pressure (a) and temperature (b) variation in the x, or stream-wise, direction in the combustor for four values of P_3 , the static pressure at the entrance to the combustor. Static temperature at the start of the combustor, T_3 , is 1300 K.

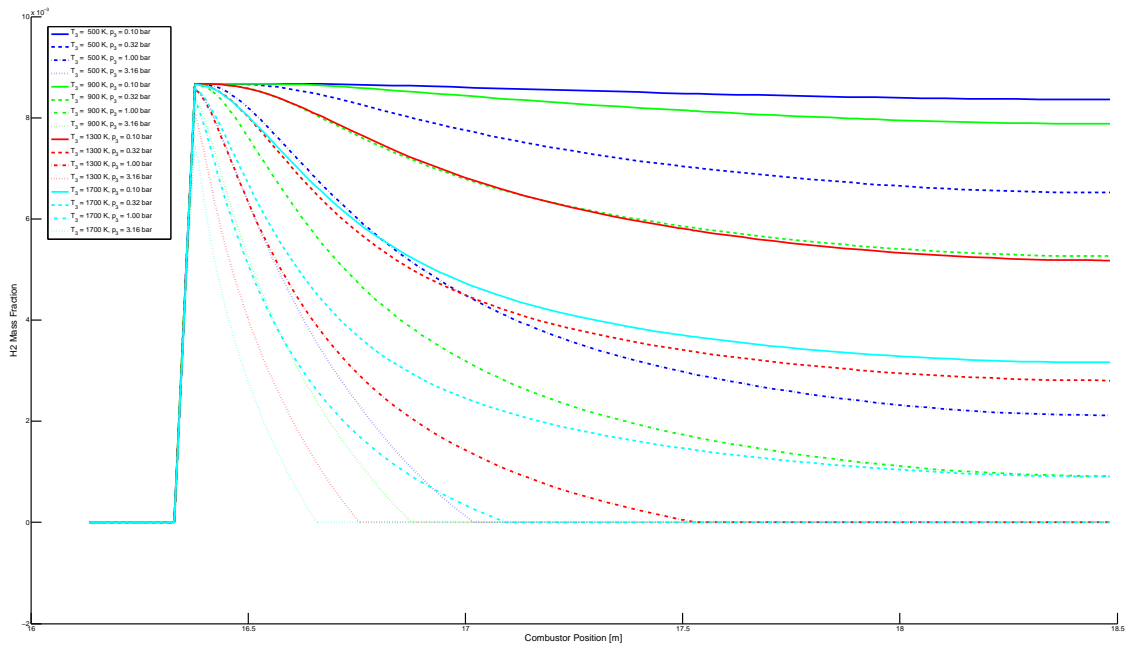


Figure 7. Hydrogen mass fraction versus stream-wise distance x .

To determine the right side of equation (17), the MASIV code computes $Y_{H_2,4}$, which is the hydrogen mass fraction at the combustor exit. Operating conditions were prescribed as follows: $T_3 = 1300$ K, $ER = 0.3$, and $U_3 = 2000$ m/s.

P_3 , the combustor inlet pressure, is varied between 0.1 and 3.16 bar. A separate chemistry lookup table was generated for each pressure value. Figure 6 shows the variation of static pressure and temperature in the flow direction in the combustor.

Combustion efficiency was computed using equation (17) and the computed profiles of H_2 mass fractions, which appear in Figure 7 for all 16 pressure and temperature combinations. The resulting plots of combustion efficiency appear in Figure 8.

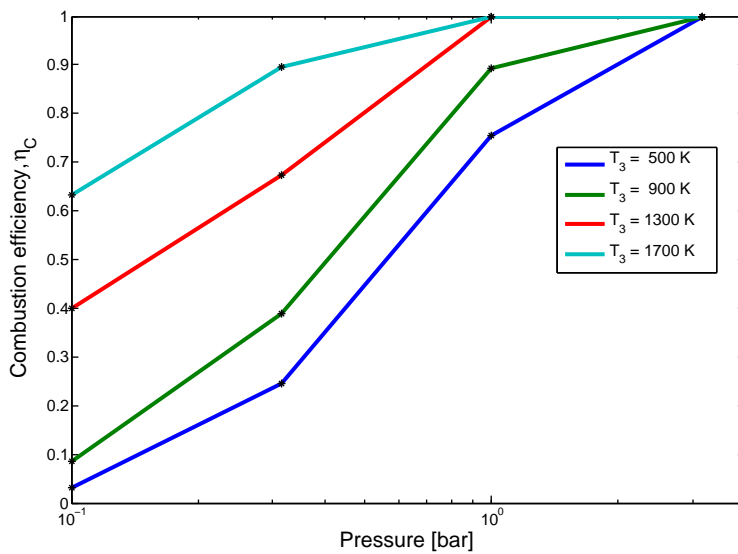


Figure 8. Combustion efficiencies computed using MASIV for different values of combustor inlet static pressures (p_3) and static temperatures (T_3).

A. Fuel Port Trade Study

To improve combustion efficiency the number (N) of fuel ports was varied. For the baseline MAX-1 geometry, the number of fuel ports is $N = 9$. The fuel ports are all placed along a single wall at one x -location. A larger combustion efficiency can be achieved by directing the fuel to a larger number of fuel ports. The total fuel flow rate is fixed by the trim requirements, and the combustor length is fixed. For a larger number of ports there will be less mass flow rate of fuel supplied to each port, so the distance required to mix and burn is reduced. It is desired to make N large enough to achieve at least 95% combustion efficiency. Figure 9 shows that the hydrogen reaction rates of the MAX-1 combustor was found, in most cases, to increase as the number of fuel ports (N) was increased from 9 to 18. However, initial results show minimal overall effect on the combustion efficiency. This trend is consistent with combustor entrance pressure conditions of $p_3 > 0.5$ bar, as shown in Figure 9a.

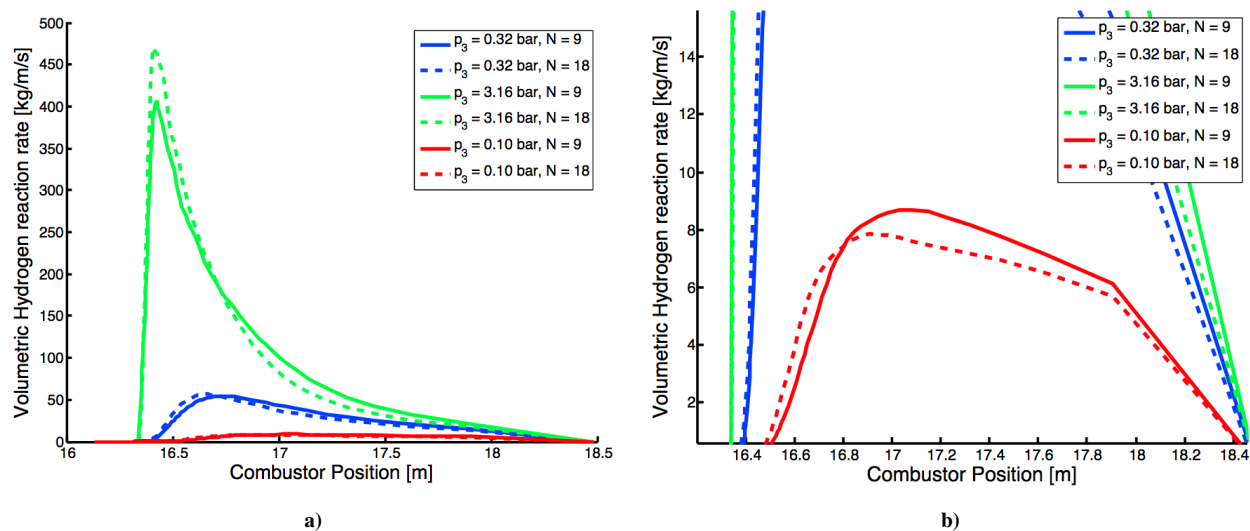


Figure 9. Effect of varying the number of fuel ports N on the hydrogen reaction rates. The solid lines represent the default geometry with $N = 9$, and the dotted lines represent fuel ports $N = 18$. Combustor entrance temperature is $T_3 = 900$ K.

In the low pressure case of $p_3 = 0.1$ bar entering the combustor, 9b, the chemical reaction rates are found to decrease, burning less fuel in the combustor. Notwithstanding the low pressure inverse trend, a practical issue with greatly increasing the number of fuel ports is how to physically locate them. Additional fuel ports could be located on all four walls of the combustor, and on cooled struts that are mounted in the flow path.

VIII. Results (b): Flameout Limits During Ascent

To compute the flameout limits using the approach described in Section II, first the reaction rate of hydrogen in the combustor is plotted as a function of x . Results were shown in Figure 5. The peak value of each of these curves yields a fuel reaction rate (RR_F) that is inserted into equation (2). Note that the peak reaction rates increase both with an increase in combustor entrance temperature and pressure; these trends are examined in Mbagwu [42].

Then, the MAX-1 vehicle was trimmed at each altitude along three ascent trajectories for which the dynamic pressure (q_∞) was equal to 50, 70, and 90 kPa, using the MASIV code. A sample trajectory is sketched in Figure 2, and the computed trajectories are plotted in Figure 10. The trim requirement is that all forces and moments be balanced; this determines the values of equivalence ratio (ER), angle of attack, and elevon settings at each altitude. These values also help to determine the combustor entrance values of air velocity (U_3), pressure (p_3), and temperature (T_3).

Experimental results were used to map flameout conditions to critical values of Damkohler number and free stream velocity in the formulation described in Section II. Takahashi et al. [43] designed an experiment to determine limits for flame-holding in a fixed-geometry scramjet combustor at off-design operating points. It was found that for the experiment run at Mach number $M = 2$ with an equivalence ratio $ER = 0.3$, step height $H = 3.6$ mm, stagnation temperature $T_{0,3} = 2000$ K, and stagnation pressure $p_{0,3} = 3.7$ atm, the flame became unstable and was subsequently blown off.

These same operating conditions were computed using the MASIV code. The maximum reaction rate of the

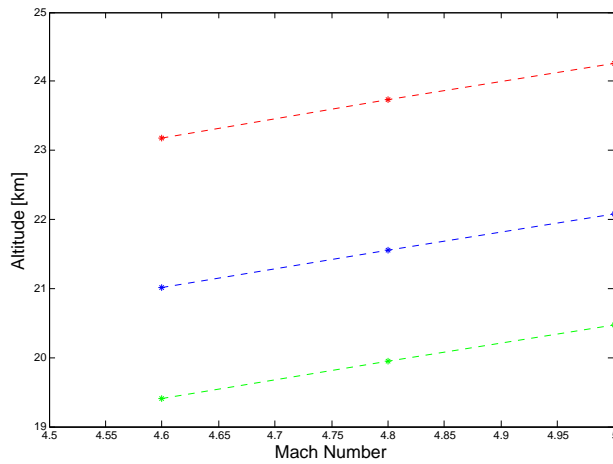


Figure 10. Ascent trajectories of dynamic pressures of $q_{\infty} = 50, 70, \text{ and } 90 \text{ kPa}$.

fuel $RR_{F,tak} = 1.1941 \text{ [1/s]}$ was then computed for Takahashi's instability point, alongside results for varying static pressures and temperatures at the same Mach number $M = 2$ and equivalence ratio $ER = 0.3$ of the original experiment. This is shown in Figure 11; the yellow starred point marks the flameout condition.

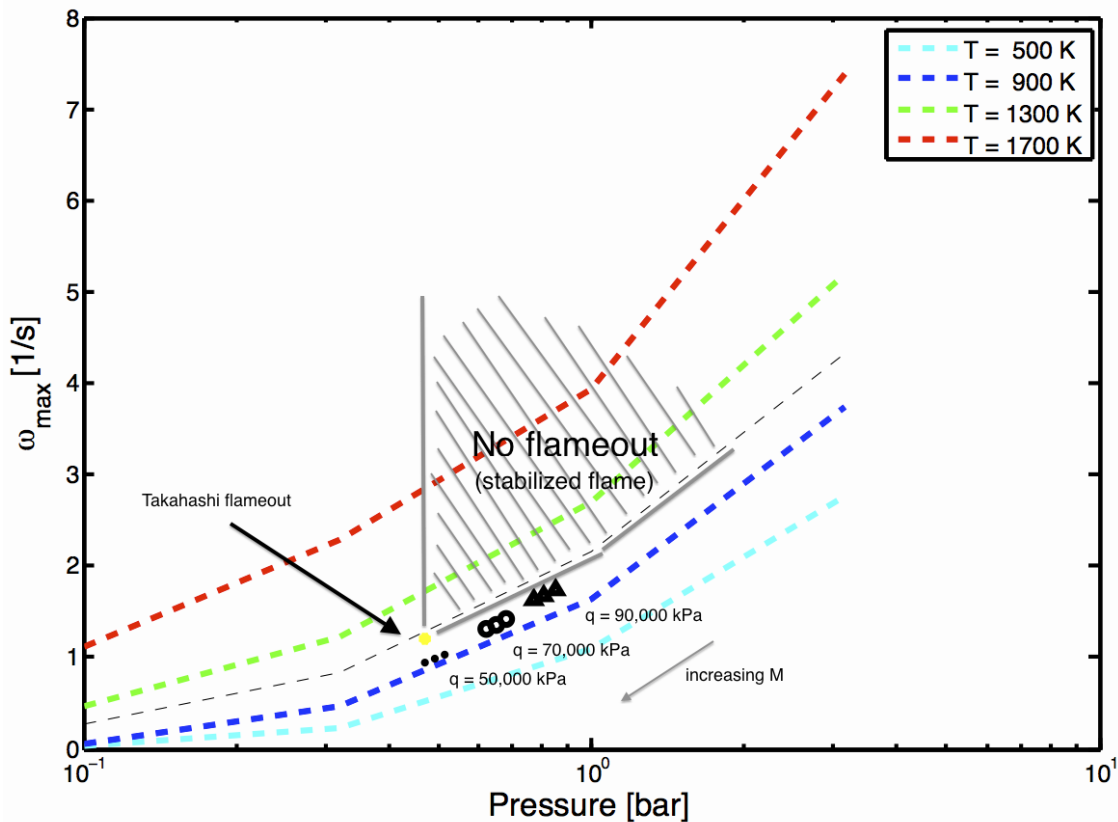


Figure 11. Map of the maximum fuel reaction rates for varying pressures and temperatures, and the computed Takahashi flameout point. The nine ascent trajectory points are also shown; increasing Mach number tends towards a region of flameout.

From the instability point, we recognize that chemical reaction rates less than this value will lead to flameout, while higher reaction rates will stabilize the flame. Previous work [42] has shown that increases in pressure and temperature

produce greater reaction rates. Thus, tracing out from the instability point, the shaded region of higher pressure and temperature is also the confident (but non-exclusive) region of flame stability. Furthermore, the nine ascent trajectory points are overlaid in Figure 11 and show that lower dynamic pressures and higher Mach numbers trend away from regions of stability and towards flameout.

The indicated region of flame stability is not exclusive; comparisons must be made to additional experiments to determine the how the instability point changes under varied conditions. These analyses will be tackled in future work.

IX. Acknowledgements

This research is funded by the Air Force Research Laboratory/Air Vehicles Directorate grant FA8650-07-2-3744 that has supported the Michigan/AFRL Collaborative Center in Control Sciences. Dr. Michael Bolender is the technical monitor. The first author also has been supported by a University of Michigan Fellowship. The authors are grateful for the technical assistance provided by Dr. Derek Dalle and Dr. Sean Torrez.

References

- [1] Dalle, D. J., Torrez, S. M., Driscoll, J. F., Bolender, M. a., and Bowcutt, K. G., "Minimum-Fuel Ascent of a Hypersonic Vehicle Using Surrogate Optimization," *Journal of Aircraft*, apr 2014, pp. 1–14.
- [2] Ozawa, R. I., "Survey of Basic Data on Flame Stabilization and Propagation for High Speed Combustion Systems," *The Marquart Co., TR AFAPL-TR-70-81*, 1971.
- [3] BAXTER, M. R. and LEFEBVRE, A. H., "Flame stabilization in high-velocity heterogeneous fuel-air mixtures," nov 1992.
- [4] Niioka, T., Kobayashi, H., Hasegawa, S., and Terada, K., "Flame stabilization characteristics of strut divided into two parts in supersonic airflow," *Journal of Propulsion and Power*, Vol. 11, No. 1, 1995, pp. 112–116.
- [5] Plee, S. and Mellor, a., "Characteristic time correlation for lean blowoff of bluff-body-stabilized flames," *Combustion and Flame*, Vol. 35, 1979, pp. 61–80.
- [6] Kundu, K. M., Banerjee, D., and Bhaduri, D., "Theoretical Analysis on Flame Stabilization by a Bluff-Body," *Combustion Science and Technology*, Vol. 17, No. 3-4, 1977, pp. 153–162.
- [7] Shanbhogue, S. J., Husain, S., and Lieuwen, T., "Lean blowoff of bluff body stabilized flames: Scaling and dynamics," *Progress in Energy and Combustion Science*, Vol. 35, No. 1, 2009, pp. 98–120.
- [8] Driscoll, J. F. and Rasmussen, C. C., "Correlation and Analysis of Blowout Limits of Flames in High-Speed Airflows," *Journal of Propulsion and Power*, Vol. 21, No. 6, nov 2005, pp. 1035–1044.
- [9] Gruber, M. R., Donbar, J. M., Carter, C. D., and Hsu, K.-Y., "Mixing and Combustion Studies Using Cavity-Based Flameholders in a Supersonic Flow," *Journal of Propulsion and Power*, Vol. 20, No. 5, 2004, pp. 769–778.
- [10] Gruber, M. R., Baurle, R. a., Mathur, T., and Hsu, K.-Y., "Fundamental Studies of Cavity-Based Flameholder Concepts for Supersonic Combustors," *Journal of Propulsion and Power*, Vol. 17, No. 1, 2001, pp. 146–153.
- [11] Rasmussen, C. C., Driscoll, J. F., Hsu, K. Y., Donbar, J. M., Gruber, M. R., and Carter, C. D., "Stability limits of cavity-stabilized flames in supersonic flow," *Proceedings of the Combustion Institute*, Vol. 30 II, No. 2, jan 2005, pp. 2825–2833.
- [12] Rasmussen, C. C. and Driscoll, J. F., "Characteristics of Cavity- Stabilized Flames in a Supersonic Flow," *Journal of Propulsion and Power*, Vol. 21, No. 2, 2005, pp. 765–768.
- [13] Zhang, T., Wang, J., Qi, L., Fan, X., and Zhang, P., "Blowout Limits of Cavity-Stabilized Flame of Supercritical Kerosene in Supersonic Combustors," *Journal of Propulsion and Power*, Vol. 30, No. 5, 2014, pp. 1–6.
- [14] Donohue, J. M., "Dual-Mode Scramjet Flameholding Operability Measurements," *Journal of Propulsion and Power*, Vol. 30, No. 3, 2014, pp. 592–603.
- [15] Bolender, M. a. and Doman, D. B., "Nonlinear Longitudinal Dynamical Model of an Air-Breathing Hypersonic Vehicle," *Journal of Spacecraft and Rockets*, Vol. 44, No. 2, 2007, pp. 374–387.
- [16] Parker, J. T., Serrani, A., Yurkovich, S., Bolender, M. a., and Doman, D. B., "Control-Oriented Modeling of an Air-Breathing Hypersonic Vehicle," *Journal of Guidance, Control, and Dynamics*, Vol. 30, No. 3, 2007, pp. 856–869.
- [17] Dalle, D. J., Fotia, M. L., and Driscoll, J. F., "Reduced-Order Modeling of Two-Dimensional Supersonic Flows with Applications to Scramjet Inlets," *Journal of Propulsion and Power*, Vol. 26, No. 3, may 2010, pp. 545–555.
- [18] Torrez, S. M., Driscoll, J. F., Ihme, M., and Fotia, M. L., "Reduced-Order Modeling of Turbulent Reacting Flows with Application to Ramjets and Scramjets," *Journal of Propulsion and Power*, Vol. 27, No. 2, mar 2011, pp. 371–382.
- [19] Torrez, S. M., Dalle, D. J., and Driscoll, J. F., "New Method for Computing Performance of Choked Reacting Flows and Ram-to-Scram Transition," *Journal of Propulsion and Power*, Vol. 29, No. 2, mar 2013, pp. 433–445.
- [20] Dalle, D. J., Torrez, S. M., and Driscoll, J. F., "Rapid Analysis of Scramjet and Linear Plug Nozzles," *Journal of Propulsion and Power*, Vol. 28, No. 3, 2012, pp. 545–555.

- [21] O'Neill, M. K. L. and Lewis, M. J., "Design tradeoffs on scramjet engine integrated hypersonic waverider vehicles," *Journal of Aircraft*, Vol. 30, No. 6, 1993, pp. 943–952.
- [22] Bowcutt, K. G., "Multidisciplinary Optimization of Airbreathing Hypersonic Vehicles," *Journal of Propulsion and Power*, Vol. 17, No. 6, 2001, pp. 1184–1190.
- [23] McQuade, P. D., Eberhardt, S., and Livne, E., "CFD-based aerodynamic approximation concepts optimization of a two-dimensional scramjet vehicle," *Journal of Aircraft*, Vol. 32, No. 2, 1995, pp. 262–269.
- [24] Starkey, R. P. and Lewis, M. J., "Critical Design Issues for Airbreathing Hypersonic Waverider Missiles," *Journal of Spacecraft and Rockets*, Vol. 38, No. 4, 2001, pp. 510–519.
- [25] Tarpley, C. and Lewis, M. J., "Stability derivatives for a hypersonic caret-wing waverider," *Journal of Aircraft*, Vol. 32, No. 4, 1995, pp. 795–803.
- [26] O', T. F., Brien, Starkey, R. P., and Lewis, M. J., "Quasi-One-Dimensional High-Speed Engine Model with Finite-Rate Chemistry," 2001.
- [27] Chavez, F. R. and Schmidt, D. K., "Analytical aeropropulsive-aeroelastic hypersonic-vehicle model with dynamic analysis," *Journal of Guidance, Control, and Dynamics*, Vol. 17, No. 6, 1994, pp. 1308–1319.
- [28] Hasselbrink, E. F. and Mungal, M. G., "Transverse jets and jet flames. Part 2. Velocity and OH field imaging," 2001.
- [29] Lumley, J. L., "The Structure of Inhomogeneous Turbulent Flows," *Atmospheric Turbulence and Radio Wave Propagation*, 1967, pp. 166–178.
- [30] Berkooz, G., Holmes, P., and Lumley, J. L., "The Proper Orthogonal Decomposition in the Analysis of Turbulent Flows," *Annual Review of Fluid Mechanics*, Vol. 25, No. 1, 1993, pp. 539–575.
- [31] Poje, A. C. and Lumley, J. L., "A model for large-scale structures in turbulent shear flows," *Journal of Fluid Mechanics*, Vol. 285, No. -1, 1995, pp. 349.
- [32] Tang, K., Graham, W., and Peraire, J., "Active flow control using a reduced order model and optimum control," *AIAA paper*, , No. June, 1996.
- [33] Romanowski, M., "Reduced order unsteady aerodynamic and aeroelastic models using Karhunen-Loeve eigenmodes," *AIAA paper*, 1996, pp. 7–13.
- [34] Kim, T., "Frequency-domain Karhunen-Loeve method and its application to linear dynamic systems," *AIAA Journal*, Vol. 36, No. 11, 1998, pp. 2117–2123.
- [35] Lucia, D. J., Beran, P. S., and Silva, W. a., "Aeroelastic System Development Using Proper Orthogonal Decomposition and Volterra Theory," *Journal of Aircraft*, Vol. 42, No. 2, 2005, pp. 509–518.
- [36] Beran, P. and Pettit, C., "Prediction of nonlinear panel response using proper orthogonal decomposition," *AIAA paper*, , No. c, 2001.
- [37] Thomas, J. P., Dowell, E. H., and Hall, K. C., "Three-Dimensional Transonic Aeroelasticity Using Proper Orthogonal Decomposition-Based Reduced-Order Models," *Journal of Aircraft*, Vol. 40, No. 3, 2003, pp. 544–551.
- [38] Kim, T., Hong, M., Bhatia, K. G., and Sengupta, G., "Aeroelastic Model Reduction for Affordable Computational Fluid Dynamics-Based Flutter Analysis," *AIAA Journal*, Vol. 43, No. 12, 2005, pp. 2487–2495.
- [39] Cao, Y., Zhu, J., Navon, I. M., and Luo, Z., "A reduced-order approach to four-dimensional variational data assimilation using proper orthogonal decomposition," *International Journal for Numerical Methods in Fluids*, Vol. 53, No. 10, apr 2007, pp. 1571–1583.
- [40] Hall, K. C., Thomas, J. P., and Dowell, E. H., "Proper orthogonal decomposition technique for transonic unsteady aerodynamic flows," *AIAA Journal*, Vol. 38, No. 10, 2000, pp. 1853–1862.
- [41] Rathinam, M. and Petzold, L. R., "A New Look at Proper Orthogonal Decomposition," *SIAM Journal on Numerical Analysis*, Vol. 41, No. 5, jan 2003, pp. 1893–1925.
- [42] Mbagwu, C. and Driscoll, J. F., "An Approach to Computing the Combustion Efficiency of a Scramjet-Powered Hypersonic Vehicle," *20th AIAA International Space Planes and Hypersonic Systems and Technologies Conference*, No. July, American Institute of Aeronautics and Astronautics, Reston, Virginia, jul 2015.
- [43] Takahashi, S., Sato, N., Tsue, M., Kono, M., Nakamura, M., Kondo, H., and Ujiie, Y., "Control of Flame-Holding in Supersonic Airflow by Secondary Air Injection," *Journal of Propulsion and Power*, Vol. 14, No. 1, 1998, pp. 18–23.